Superresolution with full-polarized tomographic diffractive microscopy

Charankumar Godavarthi,[1] Ting Zhang,[1] Guillaume Maire,*[,1] Patrick C. Chaumet,[1] Hugues Giovannini,[1] Anne Talneau,[2] Kamal Belkebir,[1] and Anne Sentenac[1]

[1]*Aix Marseille Université, CNRS, Centrale Marseille, Institut Fresnel, UMR 7249, Marseille 13013, France*
[2]*Laboratoire de Photonique et de Nanostructures, 91460 Marcoussis, France*
**Corresponding author: guillaume.maire@fresnel.fr*

Received October 23, 2014; accepted December 17, 2014;
posted December 23, 2014 (Doc. ID 225552); published January 16, 2015

Tomographic diffractive microscopy is a three-dimensional imaging technique that reconstructs the permittivity map of the probed sample from its scattered field, measured both in phase and in amplitude. Here, we detail how polarization-resolved measurements permit us to significantly improve the accuracy and the resolution of the reconstructions, compared to the conventional scalar treatments used so far. An isotropic transverse resolution of about 100 nm at a wavelength of 475 nm is demonstrated using this approach.

OCIS codes: (180.6900) Three-dimensional microscopy; (110.6955) Tomographic imaging; (110.3200) Inverse scattering; (110.1758) Computational imaging.
http://dx.doi.org/10.1364/JOSAA.32.000287

1. INTRODUCTION

Tomographic diffractive microscopy (TDM) is a powerful technique that reconstructs in three dimensions and with high resolution the refractive index map of the probed object [1]. It is also known in the literature as synthetic aperture microscopy, phase tomography, or optical diffraction tomography. Over the years, it has become more and more attractive, especially to study biological samples, since it provides at once quantitative information, three-dimensional (3D) capability, and high resolution, while remaining a label free approach [2–11]. TDM typically consists in shining a collimated laser beam on the object with different successive illumination angles (usually several hundred), and detecting for each of them the scattered far field both in phase and in amplitude. The refractive index map (or permittivity map) of the object is then reconstructed from the scattered field through a numerical inversion procedure that relies on a scattering model describing the light–sample interaction. In most cases, this model is oversimplified: the vectorial nature of the scattered field is overlooked, and the permittivity contrast of the sample is assumed to be low enough for a Born or Rytov approximation to be valid. The link between the scattered field and the sample permittivity contrast is then linear. Under these hypothesis and assuming further that the sample lies in a homogeneous infinite medium (oil or water), the image of the sample can be reconstructed by Fourier transforming the data. With this approach, the object spatial frequencies up to $2/\lambda$ are theoretically accessible. The resolution, defined as the full width at half maximum of the point spread function, can then go below the conventional diffraction limit of $\lambda/2$ and ideally reach $\lambda/4$ [12]. However, although the resolution of TDM has been shown to be better than that of bright field microscope [9] it has never reached the ideal $\lambda/4$ resolution limit [1,6,9]. A possible explanation is that the model used in the reconstruction is not precise enough and that, when aiming at the best possible resolution, the vectorial nature of the field should be accounted for.

We have recently developed a TDM in which the vectorial scattered field is recorded and processed by an inversion procedure relying on vectorial calculations of the sample–wave interaction. The image resolution obtained with the vectorial data appeared much better than that obtained with scalar data. In particular, an isotropic transverse resolution close to $\lambda/4$ was observed on nanostructured calibrated samples [13].

In this article, we detail the experimental mounting that permits the recording of the vectorial data and the inversion procedure that is able to process them. Then we describe the important calibration procedures which are mandatory to retrieve accurate and quantitative reconstructions. Finally we demonstrate the importance of the field polarization on the image resolution and accuracy on various examples.

2. EXPERIMENTAL APPARATUS AND RELATED INVERSION PROCEDURE

A. Description of the Setup

The tomographic microscope we have developed is presented on Fig. 1 [14]. It adopts a reflection configuration, so that it can be used on objects deposited on a reflective opaque substrate. Note that we have recently addressed the specific features of this uncommon configuration [15]. The light source is a supercontinuum laser (NKT Photonics SuperK Extreme EXW-12) filtered at 475 nm with a spectral width of 6 nm thanks to a variable bandpass filter (NKT Photonics SuperK Varia). The laser beam is linearly polarized and then divided into a reference beam and a beam directed toward the sample. A fast steering mirror (M, Newport FSM-300) permits control of the deflection of this latter beam, while a beam expander (BE) and diaphragm (D) generate a wide collimated beam with near

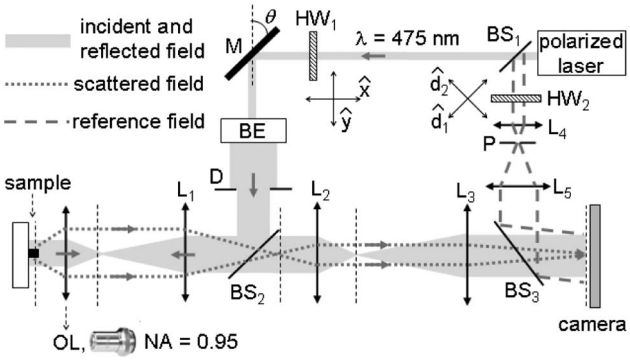

Fig. 1. Sketch of the experimental set-up: M, rotating mirror; BE, beam expander; D, diaphragm; OL, objective lens; L_1, tube lens; $L_{2,\cdots,5}$, lenses; $BS_{1,\cdots,3}$, beamsplitters; $HW_{1,2}$, half-wave plates; P, pinhole.

homogeneous power density. This beam illuminates the sample after transmission through the microscope objective (OL) and the associated tube lens (L_1). It can be locally assimilated to a plane wave since the dimensions of the object are small compared to the width of the beam. The center of the mirror is conjugated with the center of the sample through the beam expander, the tube lens, and the microscope objective. Thus, rotating the mirror varies the illumination angle without laterally shifting the beam on the object. The polar angle of the illumination can be varied over the whole numerical aperture (NA) of the objective. The field scattered by the object is collected by the microscope objective (Zeiss Epiplan-Apochromat 50×, NA = 0.95) and imaged on a sCMOS camera (Andor Zyla) after passing through relay lenses L_2 and L_3 to obtain a global magnification of about 290. After spatial filtering with a pinhole (P) and collimation, the reference field is coherently superimposed on the image field with an off-axis arrangement thanks to beamsplitter (BS_3). Off-axis holography can then be performed to retrieve the amplitude and the phase of the image field.

To carry out vectorial measurements of the scattered field, two half-wave plates have been placed in the illumination and reference arms (HW_1 and HW_2). They are used to generate two polarization bases: horizontal and vertical directions, $\hat{\mathbf{x}}$ and $\hat{\mathbf{y}}$, for the illumination arm; and along the two diagonal directions, $\hat{\mathbf{d}}_1 = (\hat{\mathbf{x}} + \hat{\mathbf{y}})/\sqrt{2}$ and $\hat{\mathbf{d}}_2 = (\hat{\mathbf{x}} - \hat{\mathbf{y}})/\sqrt{2}$ for the reference arm. These four directions are all orthogonal to $\hat{\mathbf{z}}$, which is the unit vector along the optical axis of the microscope. For an illumination polarized along $\hat{\mathbf{x}}$, successively detecting the scattered field polarized along $\hat{\mathbf{d}}_1$ and $\hat{\mathbf{d}}_2$ permits us to retrieve the vectorial scattered field. Indeed, thanks to the microscope magnification, the propagation angles of the Fourier components of the scattered field are so small in front of the camera (well below 1°), that any polarization component along $\hat{\mathbf{z}}$ can be neglected. Repeating this procedure for an illumination polarized along $\hat{\mathbf{y}}$, it is then possible to generate the vectorial scattered field for any linear polarization in the $(\hat{\mathbf{x}}, \hat{\mathbf{y}})$ plane.

In a classical TDM setup, the illumination and reference beams have the same linear polarization, and only a projection of the scattered field on this direction is measured. With our full-polarized setup, getting the vectorial scattered field for any linear polarization of the illumination requires four times more data. The measurement procedure is therefore basically four times longer but could be only twice longer using two orthogonally polarized reference beams at once [16].

In this article, we investigate samples made of nanosized resin blocks deposited on a silicon substrate. To improve the sensitivity of the reconstructions, we perform a reference measurement on the bare substrate. It permits us to measure the specular reflected field for each illumination angle. By subtracting it from the field measured in the presence of the sample, only the scattered field part remains, and the speckle noise generated by the illumination and the specular reflection is suppressed.

B. Inversion Procedure

In classical TDM, the inversion consists in applying a 3D inverse Fourier transform (FT^{-1}) to the data set [1,3–11]. This simplified approach is valid only if the following conditions are met. First, the single scattering approximation is verified. Second, the scalar approximation is valid. Third, the sample is illuminated by a plane wave and surrounded by a homogeneous medium. We have developed an inversion algorithm that overcomes all these limitations. It relies on the accurate modeling of the scattered field $\mathbf{E}_s$ with the coupled dipole method (CDM) through the two following equations:

$$\mathbf{E}_s(\mathbf{k}, \mathbf{k}_l) = \int_V \mathbf{g}(\mathbf{k}, \mathbf{r}')\chi(\mathbf{r}')\mathbf{E}(\mathbf{r}', \mathbf{k}_l)\mathrm{d}\mathbf{r}', \tag{1}$$

$$\mathbf{E}(\mathbf{r}, \mathbf{k}_l) = \mathbf{E}_{\mathrm{ref}}(\mathbf{r}, \mathbf{k}_l) + \int_V \mathbf{G}(\mathbf{r}, \mathbf{r}')\chi(\mathbf{r}')\mathbf{E}(\mathbf{r}', \mathbf{k}_l)\mathrm{d}\mathbf{r}'. \tag{2}$$

$\mathbf{k}_l$ is the wave vector of the lth illuminating plane wave, and $\mathbf{k}$ is the wave vector along which the scattered field is detected in the far field. The far field can be accessed in the setup by transferring the field measured in the image space to the Fourier space with a 2D inverse Fourier transform. The object is represented by its permittivity contrast $\chi = \varepsilon - \varepsilon_b$, where ε is the relative permittivity of the object and ε_b that of the surrounding medium, equal to 1 for the present samples placed in the air. $\mathbf{E}_{\mathrm{ref}}$ is the reference field, the one existing in the absence of the object. $\mathbf{E}$ is the total field, the sum of $\mathbf{E}_{\mathrm{ref}}$ and $\mathbf{E}_s$. $\mathbf{g}$ and $\mathbf{G}$ are, respectively, the far field and the near field Green tensors. $\mathbf{g}(\mathbf{k}, \mathbf{r}')\mathbf{p}$ is the far field emitted in the $\mathbf{k}$ direction by a dipole $\mathbf{p}$ placed at $\mathbf{r}'$ in the reference medium (which is defined as the geometry without the sample). $\mathbf{G}(\mathbf{r}, \mathbf{r}')\mathbf{p}$ is the electric field at $\mathbf{r}$ emitted by a dipole placed at $\mathbf{r}'$ in the reference medium. V is the volume of the sample. Note that when all approximations used in classical TDM are met, Eq. (1) becomes a simple 3D Fourier transform of χ.

Our iterative inversion algorithm has already been detailed in previous publications [15,17], and only its main features are recalled here. It simultaneously retrieves the sample permittivity contrast χ and the total field $\mathbf{E}_l$ in a bounded investigation domain Ω (outside Ω, χ is assumed to be null) from the set of scattered far field data $\mathbf{f}_l$, for $l = 1, \cdots, L$ illumination angles. The scattered far field is obtained on a far field surface Γ delimited by the NA of the microscope objective. The volume integrals of Eqs. (1) and (2) are performed over Ω and numerically solved by discretizing Ω into N subunits on a cubic lattice with period much smaller than the wavelength of illumination. For the sake of simplicity, symbolic notations are used for Eqs. (1) and (2), which are restated as

$$\mathbf{E}_{s,l} = \underline{\underline{B}}\chi\mathbf{E}_l, \tag{3}$$

$$\mathbf{E}_l = \mathbf{E}_{\mathrm{ref},l} + \underline{\underline{A}}\chi\mathbf{E}_l, \tag{4}$$

where $\underline{\underline{B}}$ and $\underline{\underline{A}}$ are the operators for the far field and near field Green tensors, respectively.

Starting from an initial guess provided by the backpropagation of the data set [18], χ and $\mathbf{E}_l$ are gradually adjusted at each iteration so as to minimize a cost function involving the measured data. For iteration number n, the cost function reads,

$$\mathcal{F}_n(\chi_n, \mathbf{E}_{l,n}) = W_\Gamma \sum_{l=1}^{L} \|\mathbf{h}_{l,n}^{(1)}\|_\Gamma^2 + W_\Omega \sum_{l=1}^{L} \|\mathbf{h}_{l,n}^{(2)}\|_\Omega^2, \tag{5}$$

where W_Γ and W_Ω are normalization coefficients, and $\mathbf{h}_{l,n}^{(1)}$ and $\mathbf{h}_{l,n}^{(2)}$ are two residual errors for Eqs. (3) and (4), respectively:

$$\mathbf{h}_{l,n}^{(1)} = \mathbf{f}_l - \underline{\underline{B}}\chi_n\mathbf{E}_{l,n}, \tag{6}$$

$$\mathbf{h}_{l,n}^{(2)} = \mathbf{E}_{\mathrm{ref},l} - \mathbf{E}_{l,n} + \underline{\underline{A}}\chi_n\mathbf{E}_{l,n}. \tag{7}$$

The minimization is performed with the hybrid gradient procedure described in [17].

3. NORMALIZATION PROCEDURE OF THE DATA SET

A. Principle

The polarization-resolved measurement has to be processed before providing the vectorial scattered field to the inversion procedure. The normalization procedure aims at casting the data in a form compatible with the assumptions used in the inversion procedure. First, the sample is illuminated by plane waves with unity amplitudes. Second, the phase origin for the illuminating field and for the scattered field is placed on the surface of the silicon substrate (the presence of the substrate is indeed taken into account in the inversion algorithm).

Experimentally, the phase origin is never perfectly set on the substrate. We have developed two methods to correct this phase origin mismatch, which are detailed in [15]. Once the phase origin is correctly placed, we compare the specular reflected amplitudes obtained at each illumination angle to the theoretical reflection coefficient to correct the illumination amplitude fluctuations and the different phase delays introduced on the illumination path when shifting from one angle to the other. This approach is valid if the specular reflection is not perturbed by the field scattered in the same direction by the sample, which is verified for the small objects studied here.

In the full-polarized configuration, the polarization of the illuminating beam can be initially along $\hat{\mathbf{x}}$ or $\hat{\mathbf{y}}$. In the general case, once the beam has been deflected by the fast steering mirror to an arbitrary direction $\mathbf{k}_\mathrm{i} = \sin\theta_\mathrm{i}\cos\phi_\mathrm{i}\hat{\mathbf{x}} + \sin\theta_\mathrm{i}\sin\phi_\mathrm{i}\hat{\mathbf{y}} + \cos\theta_\mathrm{i}\hat{\mathbf{z}}$, where ϕ_i and θ_i are, respectively, the azimuthal and polar angles of the illumination, the polarization of the incident field $\mathbf{E}_\mathrm{i}$ on the object can be decomposed into its S (TE) and P (TM) components:

$$\mathbf{E}_\mathrm{i} = -\cos\phi_\mathrm{i}E_\mathrm{i}\hat{\mathbf{s}} + \sin\phi_\mathrm{i}E_\mathrm{i}\hat{\mathbf{p}}, \tag{8}$$

where E_i is the complex amplitude of $\mathbf{E}_\mathrm{i}$, $\hat{\mathbf{s}} = \mathbf{k}_\mathrm{i}\times\hat{\mathbf{z}}$, and $\hat{\mathbf{p}} = \hat{\mathbf{s}}\times\mathbf{k}_\mathrm{i}$. The specularly reflected field $\mathbf{E}_\mathrm{r}$ then becomes

$$\mathbf{E}_\mathrm{r} = -r_\mathrm{S}\cos\phi_\mathrm{i}E_\mathrm{i}\hat{\mathbf{s}} + r_\mathrm{P}\sin\phi_\mathrm{i}E_\mathrm{i}\hat{\mathbf{p}}, \tag{9}$$

with r_S and r_P the reflection coefficients for S and P polarizations.

B. Normalization Factor

The field $\mathbf{E}_\mathrm{im}$ imaged on the camera is measured along the two polarization directions $\hat{\mathbf{d}}_1$ and $\hat{\mathbf{d}}_2$. $\mathbf{E}_\mathrm{im}$ is the sum of the field scattered by the object and the field $\mathbf{E}_\mathrm{r}$ reflected by the substrate. For any illumination angle, it is possible to calculate theoretically the value $\mathbf{E}_\mathrm{r}^\mathrm{th}\cdot\hat{\mathbf{d}}_p$ ($p = 1$ or 2) for the case $|E_\mathrm{i}| = 1$, as supposed in the inversion procedure. Note that in the image space of the camera, thanks to the high magnification, $\hat{\mathbf{s}}$ and $\hat{\mathbf{p}}$ can be considered in the $(\hat{\mathbf{x}}, \hat{\mathbf{y}})$ plane.

To normalize both the modulus and the phase of the data set, $\mathbf{E}_{\mathrm{im},l}\cdot\hat{\mathbf{d}}_p$ is multiplied, for each illumination l, by the factor M_l:

$$M_l = \frac{|\gamma_l| S\mathbf{E}_{\mathrm{r},l}^\mathrm{th}\cdot\hat{\mathbf{d}}_p e^{-j\varphi_l}}{2\pi\langle|\mathbf{E}_{\mathrm{im},l}\cdot\hat{\mathbf{d}}_p|\rangle_S}, \tag{10}$$

where γ_l is the projection of $\mathbf{k}_l$ on the optical axis of the microscope, and S the surface of the field of view that can be imaged on the camera. φ_l is the phase that is measured in the specular reflection direction. $\langle|\mathbf{E}_{\mathrm{im},l}\cdot\hat{\mathbf{d}}_p|\rangle_S$ is the mean modulus, averaged over the field of view, of the signal detected on the camera for the lth illumination. The object influence being limited to a small region of the image, it can be considered as the experimental value of $\langle|\mathbf{E}_{\mathrm{r},l}\cdot\hat{\mathbf{d}}_p|\rangle_S$.

The multiplication by M_l ensures that the maximal value of $|\mathbf{E}_{\mathrm{im},l}\cdot\hat{\mathbf{d}}_p|$ in the far field, which corresponds to the specular reflection, is equal to that scattered by a portion of substrate of surface S when illuminated by a plane wave with unity amplitude, as calculated by the CDM in the inversion procedure. This is the amplitude normalization part.

The phase normalization must guarantee that all the illuminating plane waves have a common phase origin placed on the substrate, as in the inversion algorithm. To experimentally fulfill this condition, the phase of the detected field $\mathbf{E}_{\mathrm{im},l}\cdot\hat{\mathbf{d}}_p$ has to be shifted by a constant, so that the phase in the specular reflection direction matches that of the theoretical Fresnel reflection coefficient. This is exactly what is performed through the multiplication by M_l.

Once this normalization has been carried out for each polarization combination in the data set ($\hat{\mathbf{x}}\hat{\mathbf{d}}_1$, $\hat{\mathbf{y}}\hat{\mathbf{d}}_1$, $\hat{\mathbf{x}}\hat{\mathbf{d}}_2$, and $\hat{\mathbf{y}}\hat{\mathbf{d}}_2$), it is possible to combine them to generate the vectorial scattered field $\mathbf{f}_l$, for any linear polarization of the illumination in the $(\hat{\mathbf{x}}, \hat{\mathbf{y}})$ plane. The inversion procedure is then launched with this vectorial data set.

4. EXPERIMENTAL RESULTS

A. Investigated Samples and Measurement Configuration

In [13], we have shown that vectorial TDM transverse resolution is significantly better than that of classical bright- or dark-field microscopes and also better than that of TDM using only scalar measurements. It reaches 160 nm for a wavelength of 632.8 nm. Here, we aim at further improving the absolute transverse resolution by using a wavelength of 475 nm, and we investigate in more details the role of polarization and the axial sensitivity.

To demonstrate the performance of our method and optical setup, we fabricated different samples as shown in Fig. 2. All

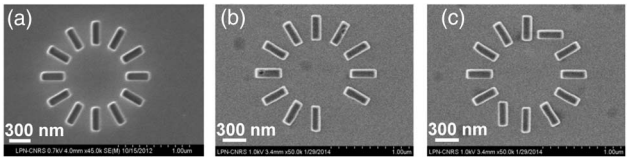

Fig. 2. Scanning electron microscope images of the investigated samples: (a) reference sample, 12 resin rods deposited on a silicon substrate; (b) sample with one missing rod; (c) sample with two misaligned rods.

the samples are made up of resin rods (relative permittivity of 2) of width 100 nm, length 300 nm, and height 140 nm, deposited on a silicon substrate. For the sample of Fig. 2(a) 12 resin rods were placed radially at the summit of a dodecagon. Hereafter this sample will be referred as the star sample. The sample of Fig. 2(b) is a star with one missing branch, and the sample of Fig. 2(c) has two of its branches misaligned in comparison to the star sample of Fig. 2(a): one top-right diagonal branch has been rotated by 60° to become horizontal, and one bottom-left diagonal branch by 30° to become vertical. All samples were illuminated by eight directions of incidence, defined by a fixed polar angle of 60° and an azimuthal angle regularly spaced within 2π.

B. Reference Star Sample

We first present the experimental results obtained with the star sample of Fig. 2(a). To point out the role of illumination and detection polarization, we present in Fig. 3 the polarized dark-field microscope images, obtained for each polarization combination ($\hat{\mathbf{y}}\,\hat{\mathbf{d}}_1$, $\hat{\mathbf{y}}\,\hat{\mathbf{d}}_2$, $\hat{\mathbf{x}}\,\hat{\mathbf{d}}_2$, and $\hat{\mathbf{x}}\,\hat{\mathbf{d}}_1$) by summing the scattered intensities recorded at the image plane for all the illuminations. One notes that the dark-field image for each polarization combination contains incomplete information about the sample; only 10 spots can be seen instead of the 12 branches of the reference star. Yet the different polarization combinations yield complementary information, since the illuminated spots are different for each case. This emphasizes the importance of full-polarized measurements in TDM for achieving isotropic superresolution instead of relying on single polarization illumination and scalar measurements.

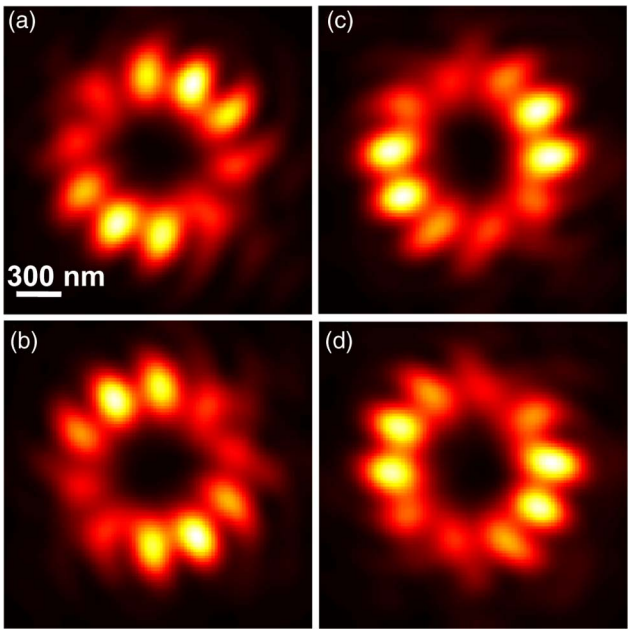

Fig. 3. Dark-field images obtained for each polarization combination in the data set: (a) $\hat{\mathbf{y}}\,\hat{\mathbf{d}}_1$ (corresponds to a polarization $\hat{\mathbf{y}}$ in the illumination path and $\hat{\mathbf{d}}_1$ in the reference path); (b) $\hat{\mathbf{y}}\,\hat{\mathbf{d}}_2$; (c) $\hat{\mathbf{x}}\,\hat{\mathbf{d}}_1$, (d) $\hat{\mathbf{x}}\,\hat{\mathbf{d}}_2$. The role of polarization in the resolution is clearly pointed out.

The transverse dark-field full-polarized image of the star sample is displayed in Fig. 4(a). It is the summation of the four polarized images of Fig. 3, and their complementary information content is highlighted since the 12 edges of the branches can now be distinguished. Figure 4(b) shows a transverse cut of the reconstruction obtained with a 3D inverse Fourier procedure applied to the TDM measurements. It assumes the data are scalar, and averages the results given by the four polarization combinations. Figures 4(c) and 4(d) present results given by the iterative inversion algorithm. For Fig. 4(c), the scattered field is scalar, projected on the polarization of the illumination, and called the $\hat{\mathbf{x}}\,\hat{\mathbf{x}}+\hat{\mathbf{y}}\,\hat{\mathbf{y}}$ scalar data set. For Fig. 4(d), the vectorial scattered field has been extracted from the full-polarized measurement and used in the inversion algorithm. To complete these results in 3D, Fig. 5 shows axial cuts (yz cuts) of the reconstructions for the 3D inverse Fourier procedure [Fig. 5(a)], the $\hat{\mathbf{x}}\,\hat{\mathbf{x}}+\hat{\mathbf{y}}\,\hat{\mathbf{y}}$ scalar inversion [Fig. 5(b)], and the vectorial inversion [Fig. 5(c)]. For the 3D FT^{-1} case [Fig. 5(a)], one notes that the axial reconstruction is particularly distorted. This is due to the presence of the reflective substrate, not taken into account by this procedure, and the small number of illumination angles [15].

The results of Figs. 4 and 5 show that the vectorial inversion provides a significantly better transverse resolution, axial sensitivity, and overall 3D permittivity map than the other methods. In particular, it resolves the interdistance between the branches at its smallest (100 nm) which is not the case for the 3D FT^{-1} and dark-field images (Fig. 4). Moreover, compared to the scalar $\hat{\mathbf{x}}\,\hat{\mathbf{x}}+\hat{\mathbf{y}}\,\hat{\mathbf{y}}$ inversion, it appears clearly that

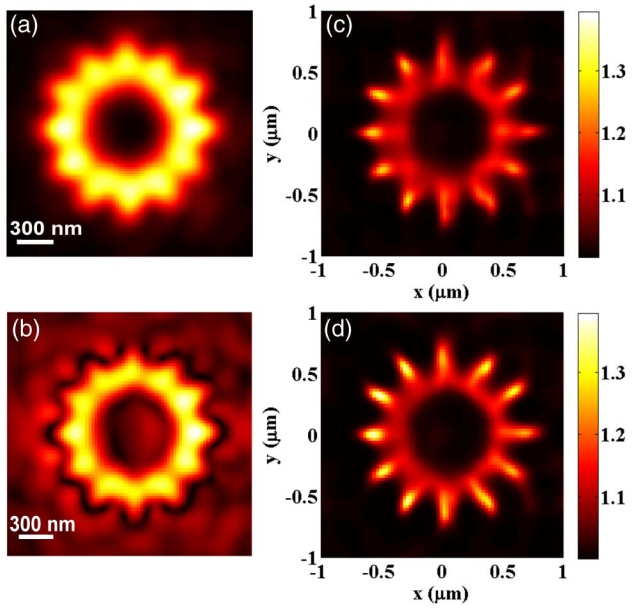

Fig. 4. Comparison of dark-field and different TDM reconstruction procedures on the transverse image of the star sample: (a) Full-polarized dark-field image. (b) Transverse cut along the center of the full-polarized 3D FT^{-1} reconstruction (modulus shown) assuming the data are scalar. (c) Transverse cut of the reconstructed permittivity averaged over the sample height using our inversion algorithm with a $\hat{\mathbf{x}}\,\hat{\mathbf{x}}+\hat{\mathbf{y}}\,\hat{\mathbf{y}}$ scalar data set. (d) Same with the vectorial data set. This latter case is significantly better than the other techniques.

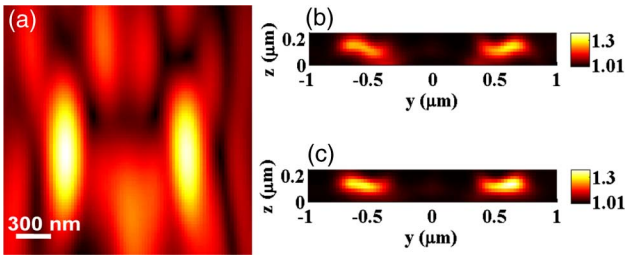

Fig. 5. Comparison of different TDM reconstruction procedures on the axial image (yz cut) of the star sample: (a) Axial cut along the center of the full-polarized 3D FT^{-1} reconstruction (modulus shown). (b) Axial cut of the reconstructed permittivity using our inversion algorithm with a $\hat{\mathbf{x}}\hat{\mathbf{x}}+\hat{\mathbf{y}}\hat{\mathbf{y}}$ scalar data set. (c) Same with the vectorial data set.

the vectorial inversion is necessary to gain an isotropic and sharper transverse resolution [Figs. 4(c) and 4(d)].

C. Sample with One Missing Branch

To pursue the demonstration of the efficiency of the vectorial inversion, we consider a nonsymmetric star sample in which a resin branch is missing [Fig. 2(b)]. The dark-field image [Fig. 6(a)], 3D FT^{-1} [Fig. 6(b)], $\hat{\mathbf{x}}\hat{\mathbf{x}}+\hat{\mathbf{y}}\hat{\mathbf{y}}$ scalar inversion [Fig. 6(c)], and vectorial inversion [Fig. 6(d)] results corresponding to the sample are presented. Although the missing branch is visible on all the images, the superiority of the vectorial inversion in terms of resolution and accuracy of the 3D permittivity map is again clearly stated.

D. Sample with Misaligned Branches

Last, we investigate the efficiency of the different imaging techniques in retrieving subtle angle misalignments between the star sample branches [Fig. 2(c)]. The different reconstructions are shown in Fig. 7. The alignment defects remain practically invisible on the dark-field image [Fig. 7(a)] and the 3D FT^{-1} reconstruction [Fig. 7(b)]. On the other hand, when the iterative inversion procedure is used, these defects can be detected. However, the vectorial inversion [Fig. 7(d)] provides once again a significant better resolution than the $\hat{\mathbf{x}}\hat{\mathbf{x}}+\hat{\mathbf{y}}\hat{\mathbf{y}}$ scalar inversion [Fig. 7(c)] and also an improved accuracy to retrieve the misaligned branches.

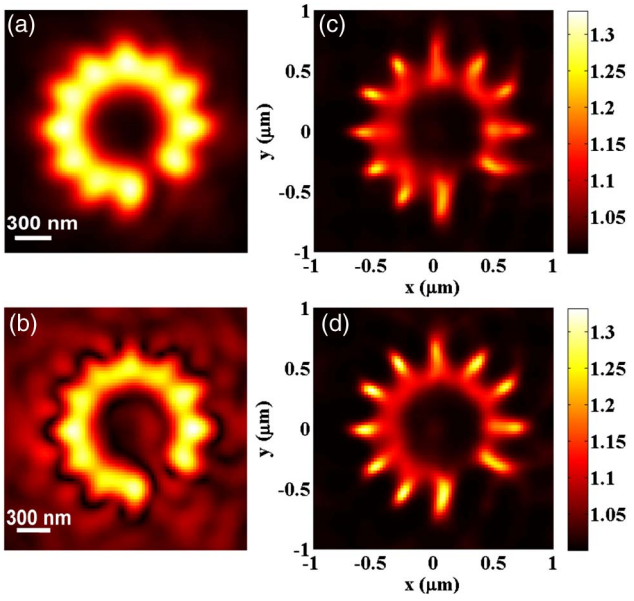

Fig. 6. Same as Fig. 4 for the sample of Fig. 2(b).

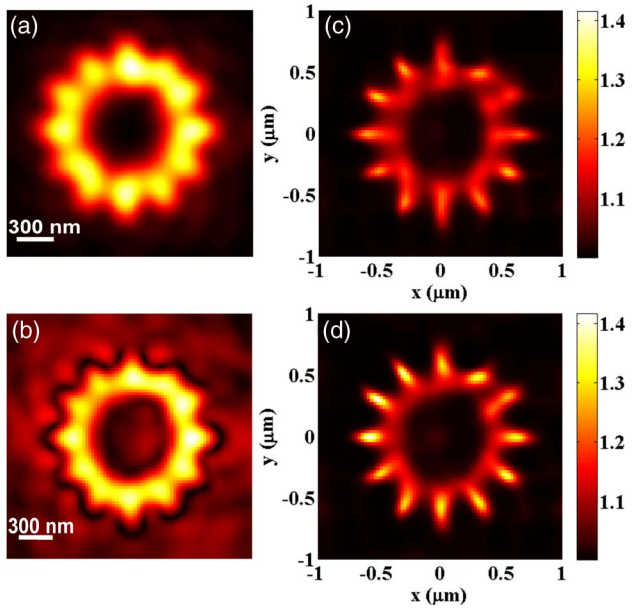

Fig. 7. Same as Fig. 4 for the sample of Fig. 2(c).

5. CONCLUSION

In conclusion, we have detailed a full-polarized TDM which enables us to reconstruct marker-free 3D samples with an unprecedented isotropic transverse resolution (about 100 nm for a wavelength of 475 nm). We have shown that using a full-polarized data set is mandatory for obtaining this isotropic transverse resolution, as well as to retrieve the geometry of the samples with an improved precision. With an appropriate calibration of the data and an inversion algorithm that takes into account the vectorial nature of the scattered field, very accurate permittivity maps of several complex samples have been retrieved along the three dimensions. The ability of our technique to discriminate very close geometries of samples has been highlighted, which is very attractive for defect characterization issues, for instance for nanotechnology components. Moreover, this work paves the way toward 3D isotropic superresolved tomography using a mirror-assisted configuration [19].

ACKNOWLEDGMENTS

This work has been financed by the ANR SURMITO, grant no. 12BS03 006 01.

REFERENCES

1. V. Lauer, "New approach to optical diffraction tomography yielding a vector equation of diffraction tomography and a novel tomographic microscope," J. Microsc. **205**, 165–176 (2002).
2. N. Destouches, C. A. Guérin, M. Lequime, and H. Giovannini, "Determination of the phase of the diffracted field in the optical domain: application to the reconstruction of surface profiles," Opt. Commun. **198**, 233–239 (2001).
3. F. Charrière, N. Pavillon, T. Colomb, C. Depeursinge, T. J. Heger, E. A. D. Mitchell, P. Marquet, and B. Rappaz, "Living specimen tomography by digital holographic microscopy: morphometry of testate amoeba," Opt. Express **14**, 7005–7013 (2006).

4. W. Choi, C. Fang-Yen, K. Badizadegan, S. Oh, N. Lue, R. R. Dasari, and M. S. Feld, "Tomographic phase microscopy," Nat. Methods **4**, 717–719 (2007).
5. M. Debailleul, V. Georges, B. Simon, R. Morin, and O. Haeberlé, "High-resolution three-dimensional tomographic diffractive microscopy of transparent inorganic and biological samples," Opt. Lett. **34**, 79–81 (2009).
6. B. Simon, M. Debailleul, A. Beghin, Y. Tourneur, and O. Haeberlé, "High-resolution tomographic diffractive microscopy of biological samples," J. Biophoton. **3**, 462–467 (2010).
7. M. Kim, Y. Choi, C. Fang-Yen, Y. Sung, R. R. Dasari, M. S. Feld, and W. Choi, "High-speed synthetic aperture microscopy for live cell imaging," Opt. Lett. **36**, 148–150 (2011).
8. Y. Sung, W. Choi, N. Lue, R. R. Dasari, and Z. Yaqoob, "Stain-free quantification of chromosomes in live celles using regularized tomographic phase microscopy," PLoS ONE **7**, e49502 (2012).
9. Y. Cotte, F. Toy, P. Jourdain, N. Pavillon, D. Boss, P. Magistretti, P. Marquet, and C. Depeursinge, "Marker-free phase nanoscopy," Nat. Photonics **7**, 113–117 (2013).
10. T. Kim, R. Zhou, M. Mir, S. D. Babacan, P. S. Carney, L. L. Goddard, and G. Popescu, "White-light diffraction tomography of unlabelled live cells," Nat. Photonics **8**, 256–263 (2014).
11. Y. Kim, H. Shim, K. Kim, H. Park, J. H. Heo, J. Yoon, C. Choi, S. Jang, and Y. Park, "Common-path diffraction optical tomography for investigation of three-dimensional structures and dynamics of biological cells," Opt. Express **22**, 10398–10407 (2014).
12. O. Haeberlé, K. Belkebir, H. Giovaninni, and A. Sentenac, "Tomographic diffractive microscopy: basics, techniques and perspectives," J. Mod. Opt. **57**, 686–699 (2010).
13. T. Zhang, Y. Ruan, G. Maire, D. Sentenac, A. Talneau, K. Belkebir, P. C. Chaumet, and A. Sentenac, "Full-polarized tomographic diffraction microscopy achieves a resolution about one-fourth of the wavelength," Phys. Rev. Lett. **111**, 243904 (2013).
14. The experiment was automatized using the free software OpticsBenchUI.
15. G. Maire, Y. Ruan, T. Zhang, P. C. Chaumet, H. Giovannini, D. Sentenac, A. Talneau, K. Belkebir, and A. Sentenac, "High-resolution tomographic diffractive microscopy in reflection configuration," J. Opt. Soc. Am. A **30**, 2133–2139 (2013).
16. T. Colomb, F. Dürr, E. Cuche, P. Marquet, H. G. Limberger, R.-P. Salathé, and C. Depeursinge, "Polarization microscopy by use of digital holography: application to optical-fiber birefringence measurements," Appl. Opt. **44**, 4461–4469 (2005).
17. E. Mudry, P. C. Chaumet, K. Belkebir, and A. Sentenac, "Electromagnetic wave imaging of three-dimensional targets using a hybrid iterative inversion method," Inverse Problems. **28**, 065007 (2012).
18. K. Belkebir, P. C. Chaumet, and A. Sentenac, "Superresolution in total internal reflection tomography," J. Opt. Soc. Am. A **22**, 1889–1897 (2005).
19. E. Mudry, P. C. Chaumet, K. Belkebir, G. Maire, and A. Sentenac, "Mirror-assisted tomographic diffractive microscopy with isotropic resolution," Opt. Lett. **35**, 1857–1859 (2010).